# Fundamental Time Scales Governing Organic Aerosol Multiphase Partitioning and Oxidative Aging

Haofei Zhang,[†,‡] David R. Worton,[†,§] Steve Shen,[‖] Theodora Nah,[‡,⊥,¶] Gabriel Isaacman-VanWertz,[†,□] Kevin R. Wilson,*[,‡] and Allen H. Goldstein*[,†,#]

[†]Department of Environmental Science, Policy, and Management, [‖]Department of Earth and Planetary Sciences, [⊥]Department of Chemistry, and [#]Department of Civil and Environmental Engineering, University of California, Berkeley, California 94720, United States

[‡]Chemical Sciences Division, Lawrence Berkeley National Laboratory, Berkeley, California 94720, United States

[§]Aerosol Dynamics Inc., 935 Grayson Street, Berkeley, California 94710, United States

**ⓢ** *Supporting Information*

**ABSTRACT:** Traditional descriptions of gas–particle partitioning of organic aerosols (OA) rely solely on thermodynamic properties (e.g., volatility). Under realistic conditions where phase partitioning is dynamic rather than static, the transformation of OA involves the interplay of multiphase partitioning with oxidative aging. A key challenge remains in quantifying the fundamental time scales for evaporation and oxidation of semivolatile OA. In this paper, we use isomer-resolved product measurements of a series of normal-alkanes ($C_{18}$, $C_{20}$, $C_{22}$, and $C_{24}$) to distinguish between gas-phase and heterogeneous oxidation products formed by reaction with hydroxyl radicals (OH). The product isomer distributions when combined with kinetics measurements of evaporation and oxidation enable a quantitative description of the multiphase time scales to be simulated using a single-particle kinetic model. Multiphase partitioning and oxidative transformation of semivolatile normal-alkanes under laboratory conditions is largely controlled by the particle phase state, since the time scales of heterogeneous oxidation and evaporation are found to occur on competing time scales (on the order of $10^{-1}$ h). This is in contrast to atmospheric conditions where heterogeneous oxidation time scales are expected to be much longer (on the order of $10^2$ h), with gas-phase oxidation being the dominant process regardless of the evaporation kinetics. Our results demonstrate the dynamic nature of OA multiphase partitioning and oxidative aging and reveal that the fundamental time scales of these processes are crucial for reliably extending laboratory measurements of OA phase partitioning and aging to the atmosphere.
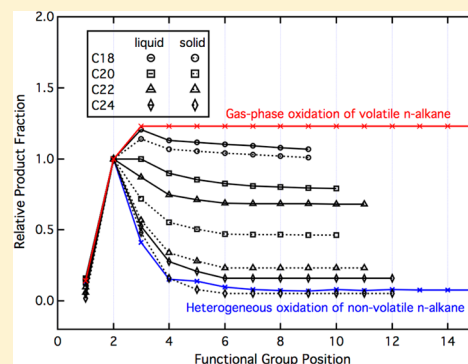
## 1. INTRODUCTION

Organic aerosols (OA) ubiquitously exist in the atmosphere with a lifetime on the order of days to weeks[1,2] and have significant impacts on air quality, climate, and human health.[3] Atmospheric OA constituents are usually semivolatile and reside in both the gas and particle phases. Traditional descriptions of gas–particle partitioning largely depend on volatility.[4−6] Current air quality models use the same approach to predict OA mass loadings in the atmosphere.[7,8] However, a substantial number of ambient measurements suggest that observed gas–particle partitioning of most OA requires more sophisticated models than volatility-based partitioning theory.[9−11] This is partly due to the chemical transformation of OA, which is dynamic and evolves with changes in both particle and atmospheric composition and conditions. As a result, partitioning is coupled to multiphase oxidative aging (i.e., chemical reactions in both phases and heterogeneously). Hence, relative time scales for partitioning and reaction control the phase in which aerosol components exist and react. In particular there are several factors that play important roles in the dynamics of multiphase partitioning with oxidative aging. For example, the volatility, viscosity, and particle size of OA govern their evaporation time scales,[12−14] while the reactivity and oxidant concentration govern the oxidation time scales. Multiphase oxidative aging increases the oxidation state of OA by various degrees based on the relative importance of gas versus particle oxidation: gas-phase oxidation occurs faster and therefore increases oxidation state more rapidly.[15] The oxidation state of atmospheric OA after short periods of oxidation (i.e., a few hours) has been observed to be higher than predictions using thermodynamic models[16−18] and laboratory studies,[19] suggesting simple extrapolation to the atmosphere that assumes time and concentration are interchangeable is not reliable.
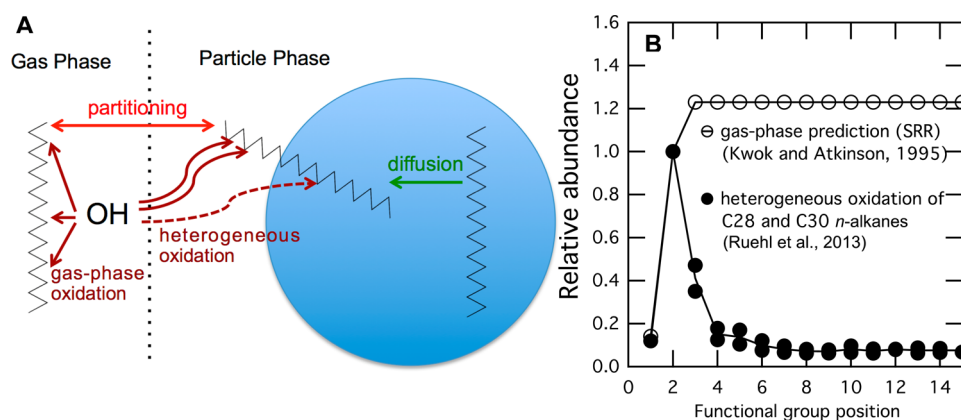
**Figure 1.** Illustrations of the atmospheric processes of semivolatile *n*-alkane aerosols. (A) Transformation of a semivolatile *n*-alkane molecule, including diffusion from inner particle to particle surface, gas−particle partitioning, and multiphase oxidation by OH radicals. H-abstraction by OH radicals in the gas phase is available at all carbon sites, but heterogeneous OH oxidation only occurs at the end of the carbon chain. (B) Relative abundance of *n*-alkane produced first-generation carbonyl and alcohol isomers from gas-phase oxidation[27] and heterogeneous oxidation of $C_{28}$ and $C_{30}$ *n*-alkanes.[30]

Therefore, quantitatively understanding how fundamental time scales of evaporation versus oxidation affect the fraction of OA oxidized in each phase is crucial to elucidating the dynamic processes in multiphase partitioning and oxidative aging, and hence improving predictions of OA mass loadings and chemical composition. Developing such quantitative representations is extremely difficult because (1) there are large uncertainties in the physiochemical characteristics of OA (e.g., volatility, viscosity, and reactivity) that often complicate accurate estimates of the fundamental time scales; (2) it is difficult to determine whether a molecule has been oxidized in the gas or particle phase; and (3) laboratory experiments and atmospheric conditions differ significantly in oxidant concentrations, so a comprehensive and validated model is needed to connect multiphase processes over a broad range of conditions.

To explore how the fundamental time scales influence the interplay of multiphase oxidation by OH and partitioning of OA, four semivolatile ($C_{18}$, $C_{20}$, $C_{22}$, and $C_{24}$) normal-alkanes (*n*-alkanes) are used as models for semivolatile hydrocarbon emissions. These compounds are primarily emitted from fossil fuel and biomass combustion sources.[20−23] Oxidation of these single-component aerosol surrogates is compared with the same set of *n*-alkanes found in a complex mixture—motor oil,[24] which better reflects the chemical complexity of primary OA.

These *n*-alkanes are used as surrogate compounds since they span a range of volatility from dominantly gas phase ($C_{18}$, vapor pressure $1.6 \times 10^{-6}$ atm at 298 K) to dominantly particle phase ($C_{24}$, vapor pressure $4.5 \times 10^{-9}$ atm at 298 K), and their physicochemical properties are well-known from the literature[10,24−29] or can be well constrained. Furthermore, it has been found that the isomeric distribution of first-generation oxidation products of *n*-alkanes depends strongly upon whether the reaction occurs in the gas phase or at the particle surface,[27,30] thus providing a clear chemical signature for tracking multiphase chemistry. For gas-phase oxidation all the C−H sites on the *n*-alkane carbon chain are available for H-abstraction (illustrated in Figure 1A). The relative H-abstraction rates (to that on the 2-position) can be estimated for gas-phase oxidation by structural reactivity relationship (SRR) as shown as open circles in Figure 1B.[27] In contrast, it was recently demonstrated that for heterogeneous reactions of nonvolatile *n*-alkanes with OH the H-abstraction occurs preferentially at the end of the carbon chain.[30] Thus, the

measured isomeric distribution formed via OH-initiated heterogeneous reactions of $C_{28}$ and $C_{30}$ *n*-alkane particles exhibits a pronounced preference for the formation of alcohol and carbonyl functional groups at the end of the molecule (Figure 1B).[30] Here, the isomeric distribution of the first-generation products is used as a sensitive probe to quantify the fraction of oxidation that occurs in either phase for semivolatile *n*-alkanes undergoing multiphase aging. In contrast, measurements of bulk properties (e.g., elemental composition) cannot provide accurate indication of the phase in which reactions occur.[31]

To quantitatively understand the interplay between thermodynamics, evaporation kinetics, and multiphase oxidation of the semivolatile *n*-alkane surrogate compounds and complex OA mixtures, a suite of measurements were conducted of total OA mass and speciated chemical composition. Particle volume changes with time (upon evaporation) and OH exposure (upon oxidation) were measured online. Isomer-resolved first-generation carbonyls/alcohols were measured off-line with a two-dimensional gas chromatograph coupled to a high-resolution time-of-flight mass spectrometer (GC × GC/HTOF-MS) with vacuum ultraviolet (VUV) photoionization. Figure 2A shows an example of $C_{18}$ *n*-alkane oxidation products separated by volatility and polarity (GC × GC). The highly dynamic processes of *n*-alkane multiphase partitioning and aging shown in Figure 1A suggest that an understanding of multiphase oxidation chemistry must be coupled with thermodynamics (volatility) and evaporation kinetics to accurately reflect the complexity of OA transformation. To investigate the mechanisms resulting in the experimental observations, we develop a kinetic model (Figure 2B) that describes the partitioning kinetics and the multiphase oxidation of semivolatile *n*-alkanes. The isomeric distributions of first-generation products, total OA mass, as well as the reactivity of the precursor *n*-alkanes are all explicitly represented in the model.

This combination of measurements and simulations provides unique constrains of multiphase partitioning and oxidative aging of the *n*-alkanes in the surrogate compound and motor oil mixture oxidation experiments. Moreover, how evaporation time scales dynamically influence oxidation products and chemical processes is quantitatively demonstrated under
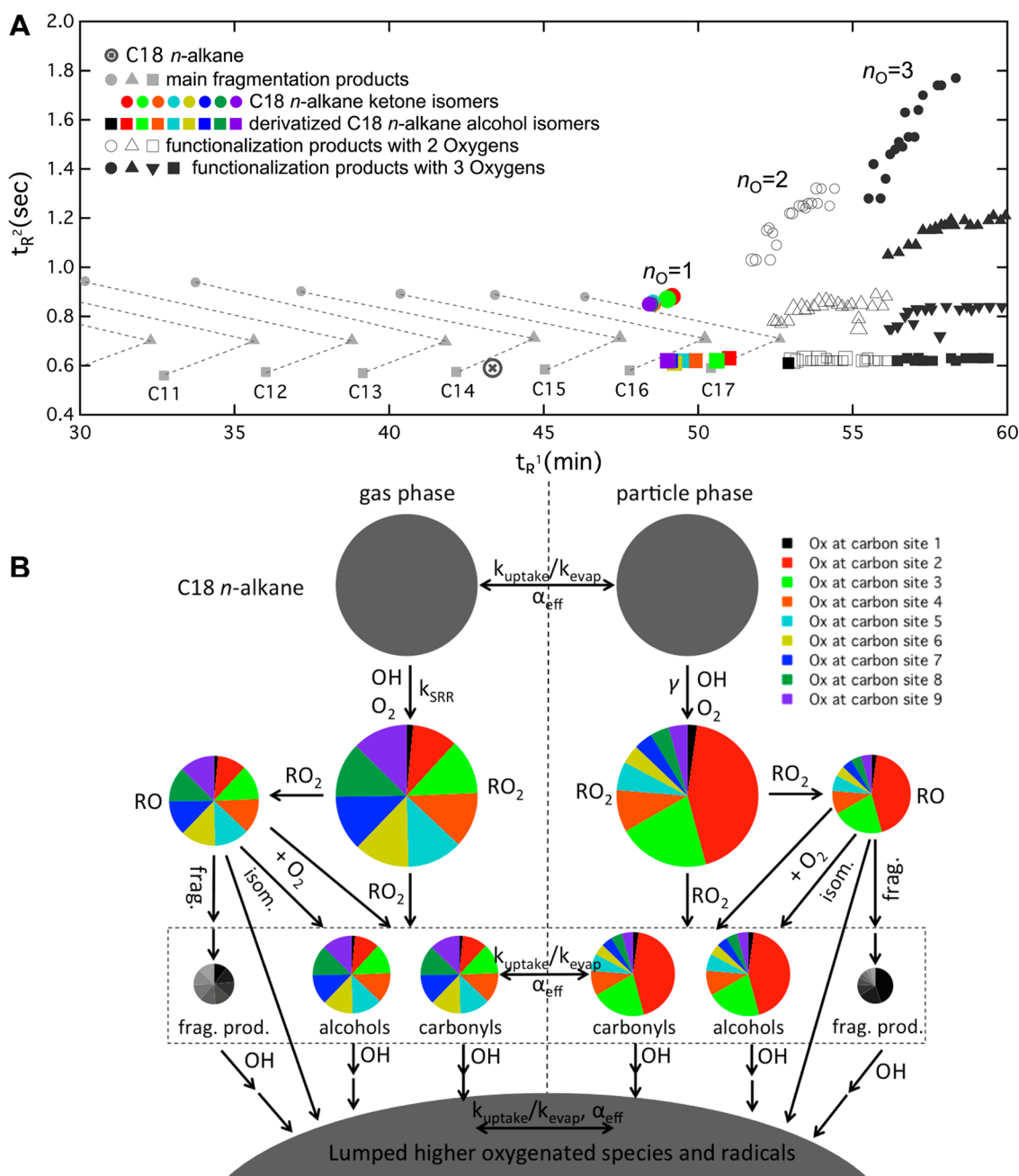
**Figure 2.** Molecular isomer resolved measurements and simulations. (A) Distribution of $C_{18}$ $n$-alkane oxidation products in the GC × GC chromatograph. Different classes of products were observed, including molecules with carbon number less than 18 (termed as fragmentation products, with the same carbon-number products lined and labeled) and functionalization products with one, two, and three oxygen atoms (in the form of carbonyl or hydroxyl groups) on the $C_{18}$ backbone. Structural isomers are resolved for the first-generation carbonyls and alcohols ($n_O = 1$) shown in various colors. (B) The conceptual framework of the semiexplicit kinetic model of $n$-alkane multiphase oxidation ($C_{18}$ $n$-alkane oxidation as an example). Gas-particle partitioning and oxidation occur simultaneously. Gas-phase oxidation and heterogeneous oxidation leads to different isomer distributions of products. The areas of circles and pies represent the relative yields of products. The formation of first-generation peroxy radicals, alkoxy radicals, carbonyls, and alcohols are represented with molecular details (radicals and functional groups on different carbon sites are shown in different colors). Further oxidation products are lumped by molecular formula. All stable products are assumed to partition between the gas and particle phases. The same colors in (A) and (B) represent functional groups on the same carbon position.

various conditions where oxidation time scales are largely distinct.

## 2. EXPERIMENTAL METHODS

**2.1. $n$-Alkane Oxidation and Evaporation Experiments.** OH-initiated oxidation experiments of $C_{18}$, $C_{20}$, $C_{22}$, and $C_{24}$ $n$-alkanes are carried out in an atmospheric pressure flow reactor (1.4 m long, 5.8 cm ID, quartz tube, Figure S1). Pure $n$-alkanes are purchased from Aldrich (Milwaukee, WI). Details of the flow reactor setup are described elsewhere.[32] Briefly, $n$-alkanes are introduced into the flow reactor by homogeneous nucleation in a $N_2$ stream, followed by a charcoal denuder to remove the gas-phase $n$-alkanes. The $n$-alkane aerosol flow is then mixed with humidified $N_2$, $O_2$, and $O_3$ before entering the flow reactor. The total flow rate is fixed at

2.0 L min$^{-1}$, corresponding to a residence time of ~110 s. The relative humidity is maintained at 30% in the flow reactor. OH radicals are generated in the flow tube reaction from the reaction of water vapor with O($^1$D), produced from ozone photolysis by mercury lamps ($\lambda$ = 254 nm, UVP, LLC.). OH exposure varies from zero to $1.4 \times 10^{12}$ molecules cm$^{-3}$ s (equivalent to up to 10-day's oxidation in the troposphere assuming a 24-h average OH concentration of $1.5 \times 10^6$ molecules cm$^{-3}$) and is calculated based upon the decay of an injected hexane tracer detected by a gas chromatograph (GC, SRI Instruments).[33] The initial particle mass concentrations measured from the outflow of the flow reactor varied from less than 10 $\mu$g m$^{-3}$ (C$_{18}$ $n$-alkane) to over 2000 $\mu$g m$^{-3}$ (C$_{24}$ $n$-alkane). The mode diameters of the normal-distributed particles are maintained at 150–250 nm in most cases. Each aerosol sample is collected for 10 min at a flow rate of 0.6 L min$^{-1}$ on quartz fiber filters (47 mm Tissuquartz, Pall Life Science, prebaked at 600 °C). The aerosol sample flow passes through a charcoal denuder (8 in. 480-channel MAST Carbon) before reaching the filters to minimize positive gas-phase artifacts caused by gas-phase adsorption to the filter media. An aerosol sample from motor oil oxidation is used from a previous study.[24]

Evaporation experiments are conducted using the similar experimental setup, but all with ammonium sulfate seed aerosols. After $n$-alkane particles coating ammonium sulfate seed aerosols (flow rate ~1.0 L min$^{-1}$) travel through the charcoal denuder, instead of passing through the flow reactor, they enter a coiled copper tube (1.025 cm ID) with 9 sampling ports evenly distributed along the tube. The length between two adjacent sampling ports is ~3.2 m, and the sampling time between each port is ~15.7 s. The total residence time in the coiled tube is ~140 s. The mode diameters of the normal-distributed particles are also maintained at 150–250 nm in all evaporation experiments. Experiments consist of collecting particle size distributions, using a SMPS, at each sampling port to measure the changing $n$-alkane particle volumes solely driven by gas−particle partitioning.

**2.2. GC × GC/HTOF-MS with VUV Photoionization.** Filter samples (1−2 punches, 0.4−0.8 cm$^2$) are thermally desorbed (in helium) into a gas chromatograph (Agilent 7890) using a thermal desorption system (TDS 3, Gerstel) with in situ gas-phase derivatization by N-methyl-N-trimethylsilyl trifluoroacetamide (MSTFA, from Sigma-Aldrich). Analytes are separated by two-dimensional gas chromatography and detected using high-resolution ($m/\Delta m \approx 4000$) time-of-flight mass spectrometry (GC × GC/HTOF-MS). Specifically, a first dimension nonpolar column (60 m × 0.25 mm × 0.25 $\mu$m, Rxi-5Sil MS, Restek Corporation) is coupled to a second dimension polar column (1 m × 0.25 mm × 0.25 $\mu$m, Rtx-200MS, Restek Corporation) by a dual-loop modulator (1.5 m × 0.25 mm Rxi guard column) that is cooled with refrigerated air from a coldfinger and periodically heated by a pulse of hot air (Zoex Corporation). The first dimension column separates compounds primarily by volatility, while the second dimension column separates compounds primarily by polarity. Electron impact (EI) ionization commonly used in GC/MS techniques tends to break molecules into many small fragments making it difficult to determine molecular weights. Isomeric compounds tend to produce a common set of fragment ions in EI and only a few unique masses, complicating their identification and separation.[34] Recent advances in GC/MS technique coupled to soft ionization such as VUV maintain minimal fragmentation

and resolve clear molecule identification.[24,30,32,34,35] In the present study, the 10.5 eV VUV source is the Chemical Dynamics Beamline (9.0.2) at the Advanced Light Source, Lawrence Berkeley National Laboratory. The beamline produces a photon intensity of $10^{15}$–$10^{16}$ photons s$^{-1}$ at a ~0.2 eV bandwidth and can be tuned from approximately 7 to 30 eV. High-resolution peak-fitting is carried out for known compounds to ensure that potential biases and incorrect mass attribution are minimized. Internal standards of deuterated C$_{12}$−C$_{36}$ $n$-alkanes are used to correct for transfer efficiency and reproducibility. Selected external standards are also analyzed for quantification purposes.[24,36] Although the molecular formulas are determined from high-resolution VUV mass spectra, only integer $m/z$ values are presented in this paper for simplicity. VUV photoionization enables most organic compounds ionized with minimal excess internal energy. For aliphatic hydrocarbons, parent molecular ions are largely maintained.[24,34,37] For oxygenated molecules with straight carbon chains and single functional group, fragmentation only occurs at the relatively weaker bonds, which is unique for each molecule.

## 3. EXPERIMENTAL RESULTS

Evaporation, repartitioning, and multiphase chemistry modify OA mass and composition dynamically. Here we report measurements of both aspects of $n$-alkane transformation, exploring OA mass change, $n$-alkane decay kinetics, and molecular-level aerosol composition. In the surrogate compound evaporation experiments without OH radicals, total OA (equal to $n$-alkanes) mass decreases as evaporation time increases (Figure 3A) for all four $n$-alkanes. As expected, the aerosol mass decreases with volatility: after 120 s 90% of C$_{18}$ $n$-alkane has evaporated while only 20% of C$_{24}$ $n$-alkane has evaporated.

In the oxidation experiments, both evaporation and oxidation occur simultaneously. The relative OA mass change as a function of OH exposure is shown in Figure 3B. When [OH] = 0, the measured OA mass is that of the particle-phase $n$-alkane after evaporation; when [OH] > 0, the measured OA mass includes both the gas-phase oxidation products of the evaporated $n$-alkane that condense onto particles (secondary OA) and products of particle-phase heterogeneous chemistry which reside in the aerosol. For the C$_{18}$ $n$-alkane oxidation experiment, the largest OA increase was observed because the largest fraction of total C$_{18}$ $n$-alkane evaporates into the gas phase. Upon oxidation, most of this gas-phase fraction of C$_{18}$ $n$-alkane forms lower volatility products that condense back to the particle phase thus greatly increasing aerosol mass. As the $n$-alkane volatility decreases, the relative OA mass change decreases since there is less gas-phase oxidation. For C$_{24}$ $n$-alkane, this ratio is less than one, because evaporation is minimal and volatilization caused by heterogeneous oxidation is more important than secondary OA condensation.

The $n$-alkane concentrations and the isomer-resolved chemical composition of their oxidation products are measured using GC × GC/HTOF-MS with VUV photoionization. The $n$-alkane aerosol decays in the surrogate compound experiments measured as a function of OH exposures are shown in Figure 3C. The reactive decays with OH exposure of the same series of $n$-alkanes from motor oil oxidation are shown in Figure 4A (The decay of C$_{18}$ $n$-alkane is not shown because its abundance is below the detection limit after oxidation).[24] For the surrogate compound experiments C$_{18}$ and C$_{20}$ $n$-alkanes show more rapid decay compared to C$_{22}$ and C$_{24}$ $n$-alkanes, even though they
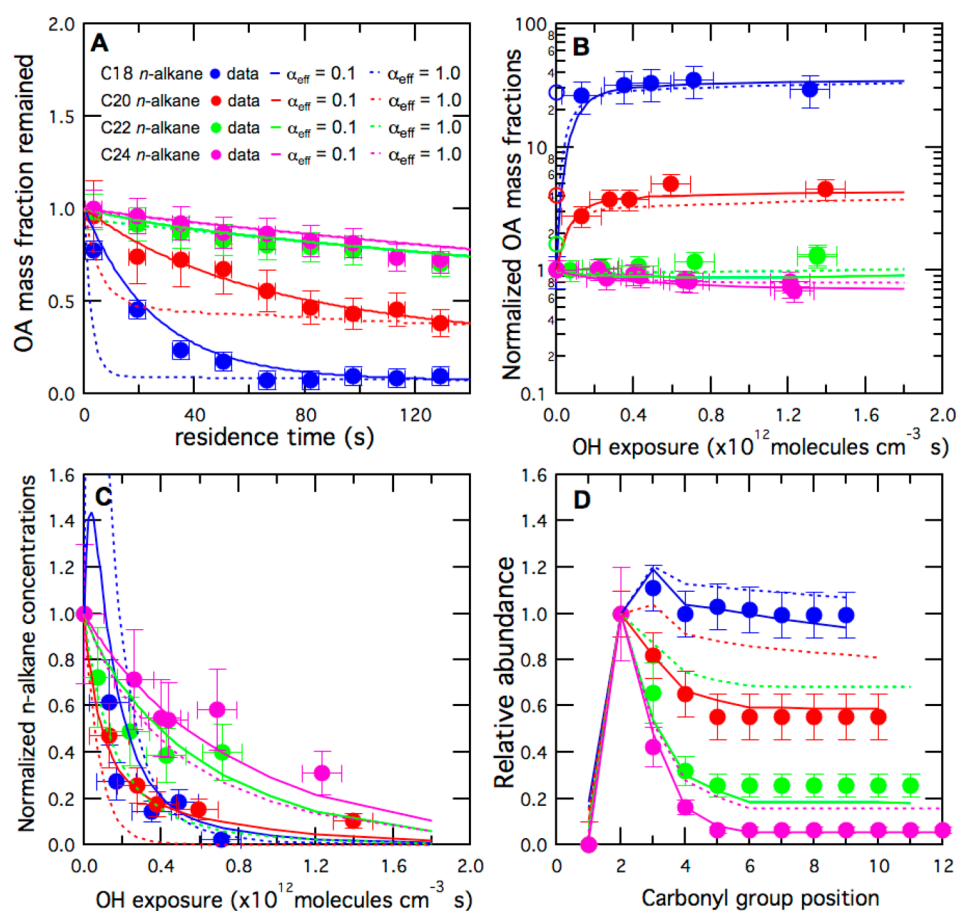
**Figure 3.** Measurement-model comparison of surrogate compound oxidation experiments. (A) Total OA mass decay as a function of evaporation time in the *n*-alkane evaporation experiments; (B) relative OA mass change as a function of OH exposure in the *n*-alkane oxidation experiments; (C) particle-phase *n*-alkane decay as a function of OH exposure in *n*-alkane oxidation experiments; (D) relative abundance of first-generation carbonyl isomers (relative to the 2-position isomers) from *n*-alkane oxidation under $[OH] = 1.3-2.1 \times 10^9$ molecules cm$^{-3}$. Data for $C_{18}$, $C_{20}$, $C_{22}$, and $C_{24}$ *n*-alkanes are represented in blue, red, green, and pink, respectively. Simulations using slow evaporation ($\alpha_{eff} = 0.1$, shown in solid lines) and fast evaporation ($\alpha_{eff} = 1.0$, shown in dashed lines) are also presented. The open circles in (B) represent the estimated initial particle-phase *n*-alkanes at the top of the flow reactor (relative to the measured mass at the bottom).

have slower reaction rates with OH in the gas phase and particle surface. This is because the overall reaction rate is a function of not only the rate constants but also the relative abundance in each phase.[12] Larger fractions of $C_{18}$ and $C_{20}$ *n*-alkanes evaporate and undergo gas-phase oxidation, which is much faster than heterogeneous oxidation.

GC × GC has the advantage over traditional GC of resolving individual compounds in a complex mixture, where different compounds with similar volatility can be sufficiently separated by polarity. For example, the $C_{18}$ *n*-alkane carbonyls and alcohols are well separated from other oxidation products (Figure 2A). The unique VUV mass spectra of isomers with functional groups on different carbons in the alkyl chain, and differences in their volatility (retention time), provide clear separation between these isomers, and their relative abundances are estimated. The detailed VUV mass spectra analyses are described in Supporting Information S1. The measured isomeric distributions of $C_{18}$-, $C_{20}$-, $C_{22}$-, and $C_{24}$-carbonyls in the surrogate compound experiments and in the motor oil oxidation experiments (under similar oxidant concentrations) are shown in Figures 3D and 4B, respectively. In both cases as the volatilities of the parent *n*-alkanes decrease (from $C_{18}$ to $C_{24}$), the distribution profile of the carbonyl isomers move from a curve similar to the gas-phase oxidation down toward the

heterogeneous oxidation curve, which is in accordance with the gas−particle partitioning theory.

In summary the experimental results are qualitatively consistent and demonstrate that volatility plays an important role governing the evaporation time scales, which influence the occurring phases of semivolatile *n*-alkane oxidation. But it is still unclear from this data set whether kinetic limitations exist within particles and how that impacts the entire dynamic system.

## 4. KINETIC SIMULATIONS

To quantitatively understand the oxidative evolution of OA mass and composition, a semiexplicit kinetic model that describes gas-phase reactions, heterogeneous reactions, as well as simplified parametrization of mass transfer between the gas-phase and particle surface was formulated. The basic structure of the model is provided in Figure 2B, and the model details are described in the Supporting Information S2. The model maintains molecular details of the first-generation peroxy radicals by assigning normalized yields of each isomer in both phases. Hence the first-generation products from radical reactions are isomer-resolved, including carbonyls, alcohols, and fragmentation products with one functional group. Further oxidation products are lumped by molecular formula, either as
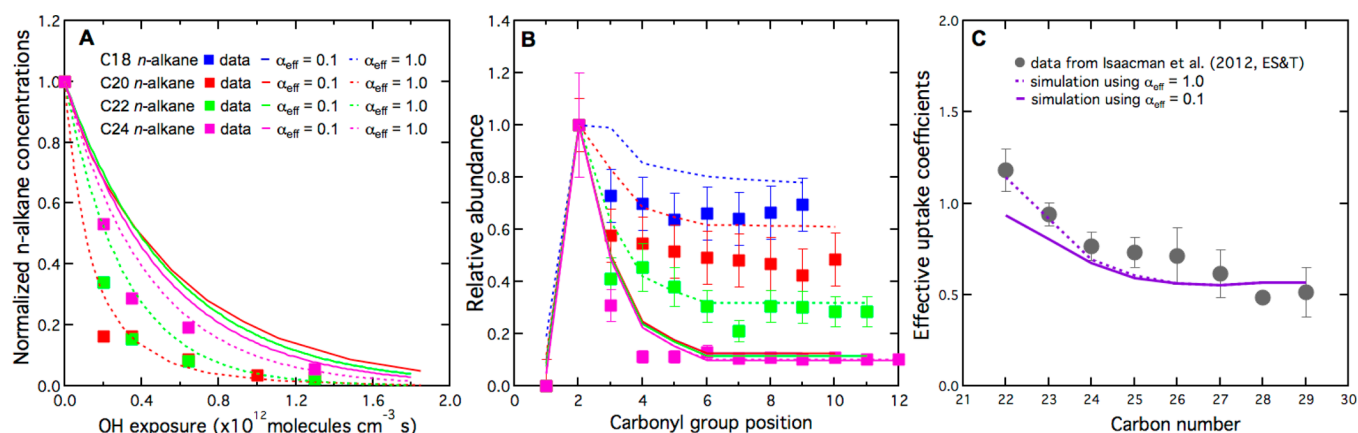
**Figure 4.** Measurement-model comparison of motor oil oxidation experiments. (A) Particle-phase *n*-alkane decay as a function of OH exposure; (B) relative abundance of first-generation carbonyl isomers (relative to the 2-position isomers) from motor oil oxidation under $[OH] = 5.4 \times 10^9$ molecules cm$^{-3}$. Data for C$_{18}$, C$_{20}$, C$_{22}$, and C$_{24}$ *n*-alkanes are represented in blue, red, green, and pink, respectively. C$_{18}$ *n*-alkane decay data were unavailable. (C) Effective OH uptake coefficients of C$_{22}$–C$_{29}$ *n*-alkane aerosols from motor oil oxidation.[24] Simulations using $\alpha_{eff} = 0.1$ (shown in solid lines) and $\alpha_{eff} = 1.0$ (shown in dashed lines) are presented with measurements.

radicals to react with the explicitly modeled first-generation peroxy radicals or as stable products that participate in gas—particle partitioning and contribute to total OA mass. Moreover, an effective evaporation coefficient ($0 < \alpha_{eff} \leq 1$) is coupled to the evaporation/uptake rate constants (i.e., constants that describe how fast gas-phase and particle-phase compounds exchange) to account for the slow partitioning caused by mass transfer limitations from particle surface to the gas phase (red arrows in Figure 1A). The effective evaporation coefficient is a combined parameter that relates to phase, viscosity, and diffusivity. Recent aerosol reaction diffusion models based on the multilayer concept explicitly treat particle-phase diffusion.[38,39] In this work, however, the main intent of the model (and the use of an effective evaporation coefficient) is not to represent all of the key elementary steps (bulk and surface diffusion, accommodation, etc.), but rather to provide an easy way to evaluate reaction vs evaporation time scales, which can be directly compared to experiments. A detailed multilayer reaction diffusion model could be more appropriate, but their complexity is beyond the scope of the paper, which really focuses on explaining the unique isomer-resolved measurements of gas- and particle-phase reactions.

To better interpret the experimental results and reveal the importance of mass transfer limitations to multiphase chemistry, $\alpha_{eff}$ is the only adjustable parameter in the model. The kinetic simulation results are compared with the measurements in Figures 3 and 4. Sensitivity analyses of other key parameters including activity coefficients, OH uptake coefficients, radical reaction rates, and branching ratios of radical reaction products are discussed in Supporting Information S3.

In each *n*-alkane aerosol evaporation experiment (Figure 3A), both rapid ($\alpha_{eff} = 1.0$) and slow evaporation ($\alpha_{eff} = 0.1$) predict similar OA fractions at 120 s. For C$_{22}$ and C$_{24}$ *n*-alkanes, $\alpha_{eff}$ only marginally affect simulation results, but for the other two more volatile *n*-alkanes, $\alpha_{eff} = 1.0$ overpredicts the quantity of evaporated mass at early stages of the experiment. This suggests that volatility determines the equilibrated OA mass fraction, but the rate at which the OA equilibrate is controlled by evaporation kinetics. The best model-measurement agreement is obtained using $\alpha_{eff} = 0.06$–$0.13$, suggesting that evaporation of solid *n*-alkane aerosols is slower than estimated for liquid

aerosol evaporation. However, it should be noted that the evaporation of pure solid *n*-alkanes could be a sublimation process, that particle-phase diffusion is irrelevant and for this case $\alpha_{eff}$ would represent a mass transfer limitation at the surface.

Simulations of the OA mass change as a function of OH (Figure 3B) using $\alpha_{eff} = 1.0$ versus 0.1 do not differ significantly from each other, and both can reasonably fit the measurements. This is because the resulting OA in both cases, although differing in detailed composition, has sufficiently low volatility to condense or stay in the particle phase at the OA mass loading in typical flow reactor experiments. Compared with the estimated initial *n*-alkane aerosol mass, the total organic particle mass after evaporation and oxidation leads to OA yields close to unity, which is consistent with earlier studies.[28]

Simulations of the *n*-alkane aerosol reactive decay in the surrogate compound experiments (Figure 3C) suggest that rapid evaporation ($\alpha_{eff} = 1.0$) predicts a faster decay than observations. This is because oxidation time scales are short and thus the oxidation rate is kinetically limited by evaporation. In contrast, the simulations of *n*-alkane aerosol decay in the motor oil oxidation (Figure 4A) suggest that the *n*-alkane aerosols evaporate faster because the particles are liquid, allowing faster mass transfer from particle surface to gas phase.

The modeled distributions of the carbonyl isomers from the four *n*-alkane surrogate compound oxidation experiments approximately replicate the measurement using $\alpha_{eff} = 0.1$. $\alpha_{eff} = 1.0$ simulations overpredict relative yields of carbonyl isomers with the functional groups in the middle of the carbon chains. This is because faster evaporation leads to more gas-phase oxidation, and thus the isomer distribution evolves toward the pure gas-phase oxidation curve. The differences in simulations between rapid and slow evaporation treatments are influenced by *n*-alkane volatility, particle mass loading, and initial fractions of gas and particle phases. In general, the differences are larger for C$_{20}$ and C$_{22}$ *n*-alkanes and smaller for C$_{18}$ and C$_{24}$ *n*-alkanes. This is consistent with the evaporation time scales being shorter for C$_{18}$ *n*-alkanes and longer for C$_{24}$ *n*-alkanes than the oxidation time scales (Figure 5A); thus, the role of the evaporation kinetics is smaller. Together with the measured isomer distributions, the model clearly demonstrates that the evaporation of solid *n*-alkane aerosols limits their multiphase
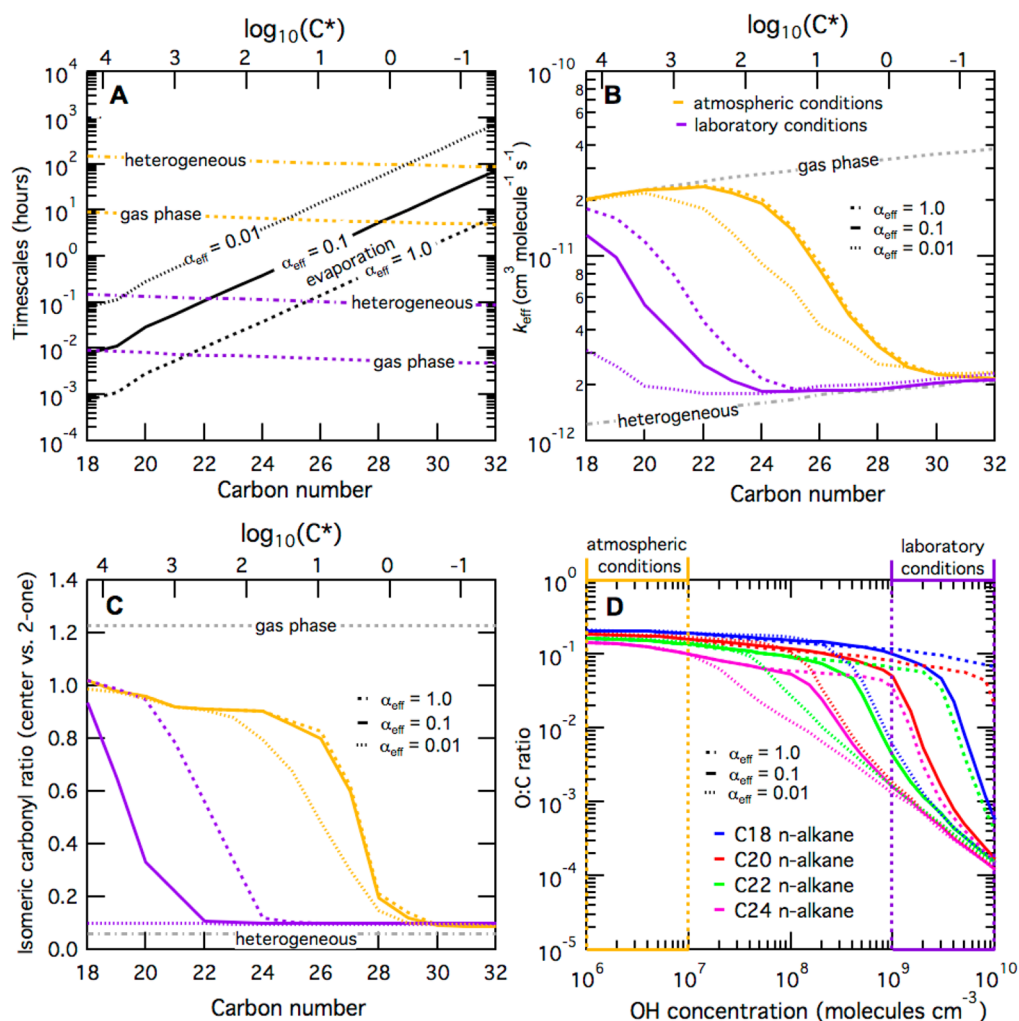
**Figure 5.** Atmospheric relevance. (A) Estimated time scales of OA aging, including the laboratory oxidation time scales in both gas and particle phases (purple lines), the atmospheric oxidation time scales in both phases (yellow lines), and the approximated evaporation time scales (black lines). (B) Simulated effective oxidation rate constants and (C) isomeric carbonyl ratios (carbonyl at the middle of carbon chain versus 2-one) at equivalently 3 days of atmospheric oxidation. In (A)−(C), estimations were made for $C_{18}$−$C_{32}$ $n$-alkanes with different $\alpha_{eff}$ values (0.01, 0.1, and 1.0). Atmospheric conditions assume [OH] = $1.5 \times 10^6$ molecules cm$^{-3}$, [OA] = 10 $\mu$g m$^{-3}$; laboratory conditions assume [OH] = $1.5 \times 10^9$ molecules cm$^{-3}$, [OA] = 1000 $\mu$g m$^{-3}$. Corresponding saturation concentrations ($C^*$) of $n$-alkanes determined by estimated vapor pressures are shown in the second $y$-axis in (A)−(C). (D) Simulated O:C ratios of aged OA from $C_{18}$−$C_{24}$ $n$-alkane multiphase oxidation under different OH concentrations but the same OH exposure levels (equivalent to 3 days of atmospheric oxidation, [OA] = 10 $\mu$g m$^{-3}$). Typical atmospheric conditions have [OH] of $1.0 \times 10^6$−$1.0 \times 10^7$ molecules cm$^{-3}$, and laboratory studies usually use [OH] higher than $1.0 \times 10^9$ molecules cm$^{-3}$. The effect of different evaporation coefficients is only distinguishable when OH concentrations are at laboratory conditions.

oxidative aging. The kinetic model is also applied to the motor oil oxidation experiments. Because the motor oil oxidation experiments used higher total OA mass loading than the $n$-alkane surrogate compound experiments, larger particle-phase fractions for the target $n$-alkanes are expected in the motor oil oxidation experiments. Therefore, the $\alpha_{eff}$ = 0.1 simulations compute carbonyl isomer distributions similar to pure heterogeneous oxidation profiles for all the $n$-alkane species. Surprisingly, the simulated distributions for the $n$-alkane carbonyl isomers in motor oil support rapid evaporation kinetics ($\alpha$ close to 1.0), in strong contrast to the solid $n$-alkane surrogate compound experiments. Isaacman et al.[24] measured the effective OH uptake coefficients of $C_{22}$−$C_{29}$ $n$-alkanes from motor oil oxidation (shown in Figure 4C). Assuming rapid evaporation ($\alpha$ = 1.0) and an OH uptake coefficient ($\gamma$) of 0.55 for the nonvolatile $n$-alkane aerosol oxidation, we can reasonably simulate the measurements; slow evaporation

treatment ($\alpha$ = 0.1) underpredicts effective OH uptake coefficients for more volatile $n$-alkane aerosol oxidation.

## 5. DISCUSSION

The decay of the parent $n$-alkane and their isomeric product distributions demonstrate that a larger fraction of the oxidation occurs in the gas phase in motor oil than in the solid $n$-alkane aerosol (if total organic mass loadings are comparable). This is probably because the mass transfer from the particle surface to the gas phase is limited in the solid particles but more efficient in the liquid motor oil particles. Explicitly representing the mass transfer process is challenging; therefore, we use an effective evaporation coefficient to describe mass transfer limitations from the particle surface to gas phases. Our conclusion that $\alpha_{eff}$ is approximately 1.0 for liquid particles and 0.1 for solid particles is in general consistent with the range provided by other studies.[40,41]

The experimental results and the models show that the fraction of semivolatile $n$-alkane aerosols oxidized in each phase is determined not only by its volatility but also by the evaporation dynamics that describes how fast they are evaporated from the particle phase to the gas phase, as well as the rate at which the molecules are chemically depleted in each phase. The estimated time scales of evaporation and oxidation of $n$-alkanes in our laboratory experiments are illustrated in Figure 5A.[12] In the laboratory oxidation experiments of $C_{18}$–$C_{24}$ $n$-alkanes ($\alpha_{eff}$ = 0.1), the time scales of evaporation (~0.01–0.3 h) and heterogeneous oxidation (~0.1 h) have similar magnitudes, and thus both processes play important roles in OA aging. The evaporation of $C_{18}$ $n$-alkane is faster than oxidation, and hence most of $C_{18}$ $n$-alkane oxidation occurs in the gas phase. In contrast, the evaporation of $C_{24}$ $n$-alkane is slower than oxidation, and hence most of $C_{24}$ $n$-alkane oxidation occurs at the particle surface. This is consistent with the isomeric results shown in Figure 3D. However, for the liquid motor oil particles, the evaporation time scales are approximately 10 times faster while the oxidation time scales remain similar. Therefore, gas-phase oxidation is more important even for the less volatile $n$-alkanes (as shown in Figure 4B). Clearly, the phase partitioning in such a dynamic system is governed by not only volatility but also the interplays between various time scales that are influenced by reactivity and viscosity as well. Wall losses of low-volatile vapors have been recently reported to greatly affect gas–particle partitioning.[42,43] However, with the high OH concentrations in the present study, the wall loss rate is smaller than oxidation by at least 2 orders of magnitude. Thus, the influence of low-volatile vapor wall loss on the fundamental time scales in this work is negligible.

The multiphase partitioning and aging of OA are expected to be quite different under atmospheric conditions due to the much smaller OH concentrations (by ~3 orders of magnitude) and longer oxidation time scales (from several hours to 5 days, shown in Figure 5A) than the laboratory experiments. Figure 5A clearly shows that heterogeneous oxidation is dominant for OA with saturation concentration ($C^*$) smaller than 100 $\mu$g m$^{-3}$ under our laboratory conditions. Evaporation is still sufficiently fast under atmospheric conditions for OA with $C^*$ = 1 $\mu$g m$^{-3}$ even when the evaporation coefficient is 2 orders of magnitude lower than unity. Thus, throughout the generally defined "semi-volatile organic compound (SVOC)" range in the atmosphere,[44] evaporation followed by subsequent gas-phase aging dominates. As we point out earlier, the main intent of the kinetic model is to provide a simple way to understand the time scales of evaporation and heterogeneous oxidation of semi-volatile $n$-alkanes. Therefore, in the cases where organics are initially formed in the gas phase (e.g., secondary OA) and get "locked" into highly viscous particles and do not readily evaporate, neither heterogeneous oxidation nor gas-phase oxidation is the major process. In this case, the evaporation time scales that also depend largely on bulk diffusivity and particle size can be much longer; thus, the model presented in this study may not be directly applicable.

Figures 5B and 5C use the kinetic model to simulate effective rate constants and first-generation carbonyl isomeric distributions (represented as the ratio of the isomers with the carbonyl group in the middle of the carbon chain versus at the 2-position) under generic atmospheric conditions ([OH] = 1.5 × 10$^6$ molecules cm$^{-3}$, [OA] = 10 $\mu$g m$^{-3}$) and laboratory conditions ([OH] = 1.5 × 10$^9$ molecules cm$^{-3}$, [OA] = 1000

$\mu$g m$^{-3}$). The simulation results indicate that large differences occur between the two conditions and the multiphase dynamics is altered by oxidant concentrations. More importantly, in the atmosphere the effect of slow or gas evaporation ($\alpha_{eff}$ = 0.1 versus 1.0) is not as distinct unless the evaporation coefficient is at least 2 orders of magnitude lower than unity (i.e., highly viscous particles). We conclude that in the atmosphere where oxidation time scales are longer than those in the laboratory, gas-phase oxidation is the dominating process even when OA evaporation is limited (within the reasonable range $0.1 \leq \alpha_{eff} \leq 1$[41]) and that laboratory oxidation experiments for semivolatile organics over shorter time scales cannot properly represent the range of oxidation products or oxidation state which occurs in the atmosphere due to the differences in the phase where the oxidation reaction occurs.

Under the same OH exposure level, gas-phase oxidation leads to more oxygenated products than heterogeneous oxidation. Figure 5D shows the elemental oxygen to carbon ratios (O:C ratios) of the aged OA from $n$-alkanes oxidation under different OH concentrations but the same overall OH exposure. Consistent with Figures 5B and 5C, the effect of evaporation coefficients only makes a difference at high OH concentrations. The simulation results also demonstrate that the O:C ratios under lower OH and longer time can be higher by several orders of magnitude than those obtained under higher OH and shorter time. Thus, a much shorter aging time in the atmosphere is required to reach a high oxidation state than is predicted by simple extrapolation of laboratory studies. Therefore, interpretations based on high-oxidant level laboratory studies must underestimate the oxygenation degree of chemical aging processes in the atmosphere, especially at short aging time scales. The simple assumption that time and concentration are interchangeable is problematic. Extrapolations from laboratory studies to the atmosphere can be reliably made if the involved time scales can be carefully measured and quantified. Understanding these fundamental time scales is crucial to estimating atmospheric processes under highly variable and dynamic conditions.

## ■ ASSOCIATED CONTENT

### Ⓢ Supporting Information

The Supporting Information is available free of charge on the ACS Publications website at DOI: 10.1021/acs.est.5b02115.

> Additional details of GC × GC/HTOF-VUV-MS analyses (S1); kinetic model description (S2 and S3); supplementary figures (Figures S1–S32) and tables (Tables S1–S4) (PDF)

## ■ AUTHOR INFORMATION

### Corresponding Authors
*Tel.: (510)-495-2474. E-mail: krwilson@lbl.gov.
*Tel.: (510)-643-2451. E-mail: ahg@berkeley.edu.

### Present Addresses
¶School of Chemical and Biomolecular Engineering, Georgia Institute of Technology, Atlanta, GA 30332.
□Department of Civil and Environmental Engineering, Massachusetts Institute of Technology, Cambridge, MA 02139.

### Notes
The authors declare no competing financial interest.

## ■ REFERENCES

(1) Rudich, Y.; Donahue, N. M.; Mentel, T. F. Aging of organic aerosol: Bridging the gap between laboratory and field studies. *Annu. Rev. Phys. Chem.* **2007**, *58*, 321−352.

(2) Pandis, S. N.; Donahue, N. M.; Murphy, B. N.; Riipinen, I.; Fountoukis, C.; Karnezi, E.; Patoulias, D.; Skyllakou, K. Introductory lecture: Atmospheric organic aerosols: Insights from the combination of measurements and chemical transport models. *Faraday Discuss.* **2013**, *165*, 9−24.

(3) Pope, C. A.; Dockery, D. W. Health effects of fine particulate air pollution: Lines that connect. *J. Air Waste Manage. Assoc.* **2006**, *56*, 709−742.

(4) Pankow, J. F. An absorption-model of the gas aerosol partitioning involved in the formation of secondary organic aerosol. *Atmos. Environ.* **1994**, *28*, 189−193.

(5) Odum, J. R.; Hoffmann, T.; Bowman, F.; Collins, D.; Flagan, R. C.; Seinfeld, J. H. Gas/particle partitioning and secondary organic aerosol yields. *Environ. Sci. Technol.* **1996**, *30*, 2580−2585.

(6) Donahue, N. M.; Robinson, A. L.; Stanier, C. O.; Pandis, S. N. Coupled partitioning, dilution, and chemical aging of semivolatile organics. *Environ. Sci. Technol.* **2006**, *40*, 2635−2643.

(7) Pye, H. O. T.; Seinfeld, J. H. A global perspective on aerosol from low-volatility organic compounds. *Atmos. Chem. Phys.* **2010**, *10*, 4377−4401.

(8) Carlton, A. G.; Bhave, P. V.; Napelenok, S. L.; Edney, E. O.; Sarwar, G.; Pinder, R. W.; Pouliot, G. A.; Houyoux, M. Model representation of secondary organic aerosol in CMAQv4.7. *Environ. Sci. Technol.* **2010**, *44*, 8553−8560.

(9) Worton, D. R.; et al. Origins and composition of fine atmospheric carbonaceous aerosol in the Sierra Nevada Mountains, California. *Atmos. Chem. Phys.* **2011**, *11*, 10219−10241.

(10) Zhao, Y.; et al. Insights into secondary organic aerosol formation mechanisms from measured gas/particle partitioning of specific organic tracer compounds. *Environ. Sci. Technol.* **2013**, *47*, 3781−3787.

(11) Isaacman, G.; Kreisberg, N. M.; Yee, L. D.; Worton, D. R.; Chan, A. W. H.; Moss, J. A.; Hering, S. V.; Goldstein, A. H. Online derivatization for hourly measurements of gas- and particle-phase semi-volatile oxygenated organic compounds by thermal desorption aerosol gas chromatography (SV-TAG). *Atmos. Meas. Tech.* **2014**, *7*, 4417−4429.

(12) Donahue, N. M.; Robinson, A. L.; Trump, E. R.; Riipinen, I.; Kroll, J. H. Volatility and aging of atmospheric organic aerosol. *Atmospheric and Aerosol Chemistry*; McNeill, V. F., Ariya, P. A., Eds.; Springer: Berlin, Heidelberg, 2014; Vol. *339*, Chap. 355, pp 97 − 143.

(13) Shiraiwa, M.; Seinfeld, J. H. Equilibration timescale of atmospheric secondary organic aerosol partitioning. *Geophys. Res. Lett.* **2012**, *39*, L24801.

(14) Shiraiwa, M.; Zuend, A.; Bertram, A. K.; Seinfeld, J. H. Gas-particle partitioning of atmospheric aerosols: Interplay of physical state, non-ideal mixing and morphology. *Phys. Chem. Chem. Phys.* **2013**, *15*, 11441−11453.

(15) Donahue, N. M.; et al. Aging of biogenic secondary organic aerosol via gas-phase OH radical reactions. *Proc. Natl. Acad. Sci. U.S.A.* **2012**, *109*, 13503−13508.

(16) Dzepina, K.; Volkamer, R. M.; Madronich, S.; Tulet, P.; Ulbrich, I. M.; Zhang, Q.; Cappa, C. D.; Ziemann, P. J.; Jimenez, J. L. Evaluation of recently-proposed secondary organic aerosol models for a case study in Mexico City. *Atmos. Chem. Phys.* **2009**, *9*, 5681−5709.

(17) Hodzic, A.; Jimenez, J. L.; Madronich, S.; Canagaratna, M. R.; DeCarlo, P. F.; Kleinman, L.; Fast, J. Modeling organic aerosols in a megacity: Potential contribution of semi-volatile and intermediate volatility primary organic compounds to secondary organic aerosol formation. *Atmos. Chem. Phys.* **2010**, *10*, 5491−5514.

(18) Lee-Taylor, J.; Madronich, S.; Aumont, B.; Baker, A.; Camredon, M.; Hodzic, A.; Tyndall, G. S.; Apel, E.; Zaveri, R. A. Explicit modeling of organic chemistry and secondary organic aerosol partitioning for Mexico City and its outflow plume. *Atmos. Chem. Phys.* **2011**, *11*, 13219−13241.

(19) Jimenez, J. L.; et al. Evolution of organic aerosols in the atmosphere. *Science* **2009**, *326*, 1525−1529.

(20) Schauer, J. J.; Kleeman, M. J.; Cass, G. R.; Simoneit, B. R. T. Measurement of emissions from air pollution sources. 2. C1 through C30 organic compounds from medium duty diesel trucks. *Environ. Sci. Technol.* **1999**, *33*, 1578−1587.

(21) Schauer, J. J.; Kleeman, M. J.; Cass, G. R.; Simoneit, B. R. T. Measurement of emissions from air pollution sources. 3. C1−C29 organic compounds from fireplace combustion of wood. *Environ. Sci. Technol.* **2001**, *35*, 1716−1728.

(22) Schauer, J. J.; Kleeman, M. J.; Cass, G. R.; Simoneit, B. R. T. Measurement of emissions from air pollution sources. 4. C1−C27 organic compounds from cooking with seed oils. *Environ. Sci. Technol.* **2002**, *36*, 567−575.

(23) Schauer, J. J.; Kleeman, M. J.; Cass, G. R.; Simoneit, B. R. T. Measurement of emissions from air pollution sources. 5. C1−C32 organic compounds from gasoline-powered motor vehicles. *Environ. Sci. Technol.* **2002**, *36*, 1169−1180.

(24) Isaacman, G.; Chan, A. W. H.; Nah, T.; Worton, D. R.; Ruehl, C. R.; Wilson, K. R.; Goldstein, A. H. Heterogeneous OH oxidation of motor oil particles causes selective depletion of branched and less cyclic hydrocarbons. *Environ. Sci. Technol.* **2012**, *46*, 10632−10640.

(25) Atkinson, R. Gas-phase tropospheric chemistry of volatile organic compounds: 1. Alkanes and alkenes. *J. Phys. Chem. Ref. Data* **1997**, *26*, 217−282.

(26) Atkinson, R. Atmospheric reactions of alkoxy and beta-hydroxyalkoxy radicals. *Int. J. Chem. Kinet.* **1997**, *29*, 99−111.

(27) Kwok, E. S. C.; Atkinson, R. Estimation of hydroxyl radical reaction rate constants for gas-phase organic compounds using a structure-reactivity relationship—An update. *Atmos. Environ.* **1995**, *29*, 1685−1695.

(28) Jordan, C. E.; Ziemann, P. J.; Griffin, R. J.; Lim, Y. B.; Atkinson, R.; Arey, J. Modeling SOA formation from OH reactions with C8−C17 n-alkanes. *Atmos. Environ.* **2008**, *42*, 8015−8026.

(29) Lambe, A. T.; Zhang, J.; Sage, A. M.; Donahue, N. M. Controlled OH radical production via ozone−alkene reactions for use in aerosol aging studies. *Environ. Sci. Technol.* **2007**, *41*, 2357−2363.

(30) Ruehl, C. R.; Nah, T.; Isaacman, G.; Worton, D. R.; Chan, A. W. H.; Kolesar, K. R.; Cappa, C. D.; Goldstein, A. H.; Wilson, K. R. The influence of molecular structure and aerosol phase on the heterogeneous oxidation of normal and branched alkanes by OH. *J. Phys. Chem. A* **2013**, *117*, 3990−4000.

(31) Lambe, A. T.; et al. Effect of oxidant concentration, exposure time, and seed particles on secondary organic aerosol chemical composition and yield. *Atmos. Chem. Phys.* **2015**, *15*, 3063−3075.

(32) Zhang, H.; Ruehl, C. R.; Chan, A. W. H.; Nah, T.; Worton, D. R.; Isaacman, G.; Goldstein, A. H.; Wilson, K. R. OH-initiated heterogeneous oxidation of cholestane: A model system for understanding the photochemical aging of cyclic alkane aerosols. *J. Phys. Chem. A* **2013**, *117*, 12449−12458.

(33) Smith, J. D.; Kroll, J. H.; Cappa, C. D.; Che, D. L.; Liu, C. L.; Ahmed, M.; Leone, S. R.; Worsnop, D. R.; Wilson, K. R. The heterogeneous reaction of hydroxyl radicals with sub-micron squalane particles: A model system for understanding the oxidative aging of ambient aerosols. *Atmos. Chem. Phys.* **2009**, *9*, 3209−3222.

(34) Isaacman, G.; et al. Improved resolution of hydrocarbon structures and constitutional isomers in complex mixtures using gas chromatography−vacuum ultraviolet−mass spectrometry. *Anal. Chem.* **2012**, *84*, 2335−2342.

(35) Gentner, D. R.; et al. Elucidating secondary organic aerosol from diesel and gasoline vehicles through detailed characterization of organic carbon emissions. *Proc. Natl. Acad. Sci. U.S.A.* **2012**, *109*, 18318−18323.

(36) Chan, A. W. H.; et al. Detailed chemical characterization of unresolved complex mixtures in atmospheric organics: Insights into emission sources, atmospheric processing, and secondary organic aerosol formation. *J. Geophys. Res. Atmos.* **2013**, *118*, 6783−6796.

(37) Worton, D. R.; et al. Lubricating oil dominates primary organic aerosol emissions from motor vehicles. *Environ. Sci. Technol.* **2014**, *48*, 3698−3706.

(38) Shiraiwa, M.; Pfrang, C.; Koop, T.; Pöschl, U. Kinetic multi-layer model of gas−particle interactions in aerosols and clouds (KM-GAP): linking condensation, evaporation and chemical reactions of organics, oxidants, and water. *Atmos. Chem. Phys.* **2012**, *12*, 2777−2794.

(39) Roldin, P.; et al. Modelling non-equilibrium secondary organic formation and evaporation with the aerosol dynamics, gas- and particle-phase chemistry kinetic multiplayer model ADCHAM. *Atmos. Chem. Phys.* **2014**, *14*, 7953−7993.

(40) Saleh, R.; Khlystov, A.; Shihadeh, A. Determination of evaporation coefficients of ambient and laboratory-generated semi-volatile organic aerosols from phase equilibration kinetics in a thermodenuder. *Aerosol Sci. Technol.* **2012**, *46*, 22−30.

(41) Saleh, R.; Donahue, N. M.; Robinson, A. L. Time scales for gas−particle partitioning equilibration of secondary organic aerosol formed from alpha-pinene ozonolysis. *Environ. Sci. Technol.* **2013**, *47*, 5588−5594.

(42) Zhang, X.; Cappa, C. D.; Jathar, S. H.; McVay, R. C.; Ensberg, J. J.; Kleeman, M. J.; Seinfeld, J. H. Influence of vapor wall loss in laboratory chambers on yields of secondary organic aerosol. *Proc. Natl. Acad. Sci. U.S.A.* **2014**, *111*, 5802−5807.

(43) McVay, R. C.; Cappa, C. D.; Seinfeld, J. H. Vapor-wall deposition in chambers: Theoretical considerations. *Environ. Sci. Technol.* **2014**, *48*, 10251−10251.

(44) Donahue, N. M.; Epstein, S. A.; Pandis, S. N.; Robinson, A. L. A two-dimensional volatility basis set: 1. organic-aerosol mixing thermodynamics. *Atmos. Chem. Phys.* **2011**, *11*, 3303−3318.